Adv Syst Sci Appl 2025; **3**; 52-73

Analysis of the Thermal Behavior of a Workspace in the Adrar Region

Oudrane Abdellatif[1*], Aour Benaoumeur[2],
Bada Abdelmalek[1,3], Kheiri Abdelhamid[4]

[1]) Ahmed Draïa University of Adrar, Adrar, Algeria
[2]) National Polytechnic School of Oran, Oran, Algeria
[3]) University of Science and Technology of Oran, Bir El Djir, Algeria
[4]) University of Lorraine, Lorraine, France

Abstract: This study presents an experimental and numerical investigation of the thermal behavior of a workplace located in the Adrar region. Temperature variations within the building were analyzed through a detailed modeling approach and validated using data collected during a 20-day experimental campaign conducted in May 2024. All modes of heat transfer were considered, and energy balance equations were formulated for each structural material. The resulting system of equations was solved using an implicit finite-difference scheme combined with the Gauss algorithm and an iterative procedure, accounting for the dependence of convective and radiative heat-transfer coefficients on the surrounding temperatures. Numerical results indicate that the thermal conductivity of the heavy concrete bricks, together with the local climatic conditions, significantly contributes to indoor temperature increases. Comparison of numerical predictions with experimental measurements for two representative days (May 10 and May 18, 2024) demonstrated excellent agreement, with errors not exceeding 4%. The findings provide insights into the thermal performance of public buildings in the Adrar region and offer a reliable numerical tool for engineers to select appropriate construction materials. The study also highlights that modern building materials, when used without adequate thermal insulation, can lead to excessive indoor temperatures and uncontrolled energy consumption in this desert environment.

Keywords: Habitable construction, Thermal behavior, Workplace, Heat convection, Thermal conductivity, Building materials, Desert areas, Internal temperature.

Nomenclatures

Cp	Specific heat	$J.Kg^{-1}.K^{-1}$
e	Material thickness	m
F_i	Geometric form factor	-
I	Electric current intensity	mA
hr	Radiation heat exchange coefficient	$W.m^{-2}.k^{-1}$
h_{conv}	Convection heat exchange coefficient	$W.m^{-2}.k^{-1}$
h_{cext}	External heat exchange coefficient for convection	$W.m^{-2}.k^{-1}$
L	Length	m
m_{ps}	Mass of the South wall	Kg
Q_{CCv}	Amount of heat exchanged by convection	W
Q_{door}	Amount of heat exchanged by the door	W
Q_{wall}	Amount of heat exchanged by the wall	W
Q_{absor}	Amount of heat absorbed	W
Q_{source}	Amount of heat from the source	W
q_r	Amount of radiative flux	$W.m^{-2}$
φ	Heat flux density	$W.m^{-2}$
R	Electrical resistance	Ω
S_{PS}	South wall surface	m^2
T_{amb}	Room temperature	°C
T_{ground}	Soil temperature	°C
T_{air}	Air temperature	°C
T_{ext}	External temperature	°C
T_{int}	Internal space temperature	°C

---

[*] Corresponding author: abdellatif.habadat@gmail.com, +213662830459

ΔT	Temperature deviation	$°C$
T_{VC}	Temperature of the celestial vault	$°C$
T_{PSI}	Internal south wall temperature	$°C$
T_{PNI}	Temperature of the internal north wall	$°C$
T_{PFPI}	Internal temperature of the wall ceiling	$°C$
U_{glas}	Surface thermal transmittance coefficient of glass	$W.m^{-2}.\ K^{-1}.J^{-1}$
V_{air}	Air volume	m^3
V_{wind}	Average wind speed	$m.\ s^{-1}$
Lettres Grecques		
α	Absorption coefficient	-
ε	Emissivity coefficient	-
λ	Thermal conductivity	$W.m^{-1}.K^{-1}$
ρ	Density	$Kg.m^{-3}$
σ	Stefan-Boltzmann constant	$W.\ m^{-2}.\ K^{-4}$
Nombres Adimensionnels		
Gr	Grashof number	-
Pr	Prandtl number	-
Ra	Rayleigh number	-
Abreviation		
PS	South wall	-
PN	North wall	-
PE	East wall	-
PO	West wall	-
PFP	Ceiling wall	-
PSI	Internal south wall	-
PNI	Internal north wall	-
PEI	Internal east wall	-
POI	Internal west wall	-
PFPI	Internal ceiling wall	-
PSE	External south wall	-
PNE	External north wall	-
PEE	External eat wall	-
POE	External west wall	-
PFPE	External ceiling wall	-
HTC	Building heat transfer coefficient	-
DPS	Date palm spikelet	-
DPF	Recycled date palm fiber	-
DPP	Petiole of the date palm	-
XPS	Panneau de polystyrène extrudé	-
PCM	Phase change materials	-
HTR	Hourly temperature reduction	-
HHGR	Hourly reduction in heat gain	-
ECA	Evaporative air conditioning	-
NV	Natural ventilation	-

1. INTRODUCTION

Quantifying thermal exchanges between buildings and their surrounding environment at the urban scale requires a detailed understanding of local energy balances across multiple levels, from districts and building clusters down to individual structures and specific building components. The multiscale nature of this problem makes optical sensor technologies particularly relevant, as they enable non-contact spatial measurements that remain effective at various scales. Recent advances in sensor technology have enhanced the resolution of detection matrices and improved associated optical systems, allowing for more precise analysis of observed scenes. The luminance measured by these sensors originates from multiple elements within the field of view, from which surface temperatures of the urban environment can be inferred [1,2].

Establishing the relationship between measured luminance, the temperature of individual components, and heat transfer through building envelopes requires comprehensive modeling of the underlying physical phenomena [1,3,4]. These mechanisms are highly interdependent, as surface energy balances are strongly influenced by local climatic conditions. A review of existing methods for quantifying thermal exchanges in buildings indicates that their development has been largely shaped by methodological choices, attracting growing interest from the scientific community concerned with energy storage and conservation. Several representative studies are highlighted below for illustrative purposes.

Kumaraswamy et al. [5] investigated thermal storage in building materials and long-term energy conservation using phase-change materials (PCM). Due to their latent heat capacity, PCMs can store significant amounts of heat or cold within limited volumes, reducing fluctuations in indoor air temperature and maintaining thermal comfort over extended periods. Selecting an appropriate PCM, however, requires careful consideration of local climatic constraints. Kaoutari et al. [6] conducted numerical and experimental analyses of coupled heat and moisture transfer in a biobased double-layer wall system, integrating measured material properties into a dynamic model based on the approaches of Künzel and Mendes. Finite-difference methods were employed to solve the coupled transfer processes, with transient simulations representing real winter and summer conditions. Comparisons demonstrated that experimental data provided highly accurate solutions.

Virginia et al. [7] examined uncertainties associated with co-heating tests to evaluate the impact on estimated building Heat Transfer Coefficients (HTC), showing that weather conditions, complex building designs, and experimental practices can significantly influence HTC estimates. Belatrache et al. [8] explored the use of date palm waste as insulating material in arid climates, demonstrating reductions in cooling electricity consumption of up to 64.7% compared to traditional constructions. Laidi et al. [9] assessed energy performance of a single-family house with a mansard roof in Algeria, showing that attics, insulated or not, contribute to reduced cooling demand across various climatic zones. Jiang et al. [10] modified clay walls with cement, gravel, sand, and polypropylene fibres, highlighting the strong heat and moisture buffering capacity of the modified walls, reducing indoor temperature and humidity fluctuations.

Chaoping et al. [11] studied thermal optimization of traditional rural dwellings in northeastern Sichuan, comparing four wall renovation strategies through numerical simulations. Central insulation combined with extruded polystyrene (XPS) panels significantly improved indoor thermal comfort. Qudama et al. [12] investigated compacted PCMs integrated into building envelopes under warm climates, achieving hourly temperature and heat gain reductions of up to 15.1% and 34.9%, respectively, and lowering indoor temperatures by up to 4 °C. Yadeta et al. [13] conducted a field survey of thermal comfort in 104 dwellings, producing adaptive comfort models essential for designing sustainable dwellings in regions with limited energy access. Guo et al. [14] performed on-site studies of office buildings in Turpan, China, under evaporative cooling and natural ventilation, revealing discrepancies with current adaptive comfort standards and providing guidance for updating design parameters and passive strategies.

Building on these insights, the present study investigates the thermal behaviour of a workplace in the Adrar region of southern Algeria. An experimental campaign conducted in May 2024 over 20 days was implemented to validate the numerical results obtained from a thermal model developed for this work. Temperature and humidity measurements (Testo 175T2, Testo 175T3, and Testo 174H) included interior surface temperatures of south and north walls, interior roof surface temperature, indoor air temperature, indoor relative humidity, and outdoor air temperature.

To achieve the stated objectives, this work is structured as follows. A description of the studied workplace, serving as an office for a university lecturer, is provided in Section 1, followed by the climatic characteristics of the Adrar region in Section 2. Section 3 details the measurement instruments and the simplifying assumptions adopted in the experimental protocol. The mathematical modeling of the energy balance is introduced in Section 4, and finally, Section 5 presents a comprehensive analysis of the results along with a comparison between experimental observations and numerical predictions based on a typical day.

2. EXPERIMENTAL STUDY ELEMENT

The workspace under study corresponds to the office of a university professor. In the numerical model, the room is idealised as a rectangular control volume, as shown in Figure 2.1. The enclosure comprises one external door and one glazed opening. All façades of the office are unobstructed and directly exposed to solar radiation throughout the day, implying that both shortwave and longwave radiative exchanges occur without shading effects.

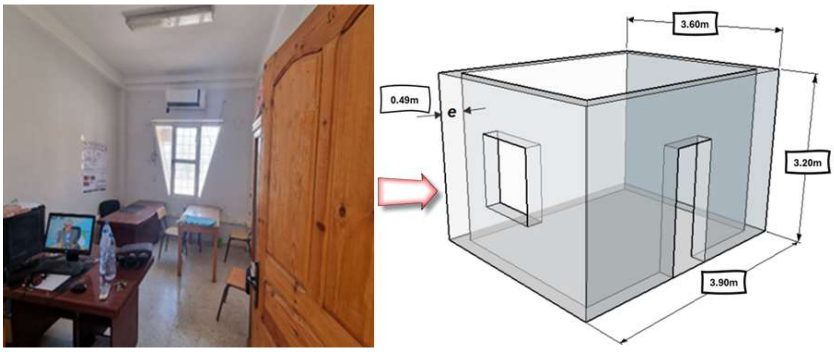

Fig. 2.1 View and geometric dimensions of the workplace

2.1. Geometrical and Physical Properties of the Workplace

The experimental workspace was designed considering both its geometric configuration and physical properties, which serve as input parameters for the thermal model. These characteristics were defined in accordance with civil engineering practices appropriate for desert climates. The external walls are composed of a double-layer masonry construction with a total thickness of 49 cm, incorporating a 5 cm air cavity that functions as thermal insulation. All surfaces are assumed to be homogeneous and isotropic for thermal calculations. Table 2.1.1 provides a detailed overview of the geometric dimensions of the experimental element.

Table 2.1.1. Geometric dimensions of the workplace

	Width (m)	**Length (m)**	**Height (m)**	**Thickness (m)**	**Surface (m^2)**
South wall	3.60	3.60	3.20	0.49	12.96
North Wall	3.60	3.60	3.20	0.49	12.96
East Wall	3.90	3.90	3.20	0.49	15.21
West Wall	3.90	3.90	3.20	0.49	15.21
Ceiling tile	3.60	3.90	-	0.20	14.04
Floor Slab	3.60	3.90	-	0.22	14.04

Table 2.1.2 summarizes the construction materials assigned to each wall of the experimental workspace, along with their relevant thermophysical properties, which are used as input parameters in the numerical thermal model.

Table 2.1.2 Construction materials of the workplace

	South wall	North Wall	East Wall	West Wall	Ceiling tile	Floor Slab
Materials	Double wall in red brick + exterior coating + air blade + Interior coating	Red brick + Exterior coating+ Interior coating	Red brick + exterior coating+ Interior coating	Red brick + exterior coating+ Interior coating	Concrete Brick (Hourdis) + reinforced concrete + Interior coating+ exterior coating	Granite tiles + Heavy concrete

Building materials with appropriate physical and thermal properties are essential for accurately simulating heat transfer. Accordingly, these properties have been carefully determined to enable precise modelling of the various thermal exchanges. Table 2.1.3 presents the physical and thermal properties of all materials used in the study:

Table 2.1.3. Physical and thermal properties of building materials [15-18]

	ρ (Kg. m^{-3})	Cp (J.Kg^{-1}.K^{-1})	λ (W.m^{-1}.K^{-1})	ε	α
Red brick	300	800	0.08	0.93	0.60

Hourdis brick	1800	1000	1.15	0.97	0.60
Reinforced concrete	2400	1000	2	0.97	0.60
Heavy concrete	2300	1000	2.71	0.97	0.60
Cement + Earth + Red paint	1959	1.492	0.671	0.95	0.75
Plaster	850	936	0.35	0.97	0.21
Granite tiles	2200	936	2.1	0.97	0.58
Air gap	1.200	1000	0.04	0.40	0.40
Glazing	130	720	2.50	0.89	0.08

Figure 2.1.1 illustrates the detailed geometric configuration of the external wall section considered in the experimental study.

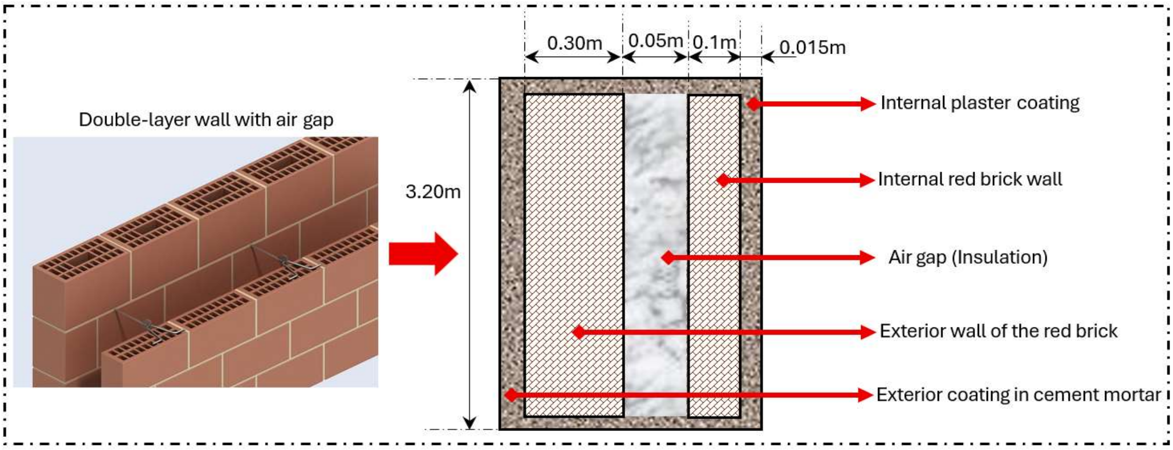

Fig. 2.1.1. Engineering of the structure of a wall with two walls separated by an air gap

3. DESCRIPTION CLIMATIC OF THE ADRAR REGION

The present study was conducted in Adrar, located in the southwest of Algeria, covering an area of 424.948 km² with a population of 402,197 inhabitants according to the 2008 census (see Figure 3.1). The region possesses significant potential for renewable energy exploitation, particularly solar and wind resources [19-22]. Adrar's climate is classified as hot desert (BWh) according to the Köppen system [23,24], characterized by extreme aridity, low and irregular precipitation (annual average <50 mm), and prolonged periods of high ambient temperatures, often exceeding 45 °C during summer months. Relative humidity remains very low, typically below 20%, while annual global solar irradiation is exceptionally high, exceeding 2,800 kWh/m²/year. These climatic conditions result in substantial solar and convective heat loads on building envelopes, which are critical parameters for thermal modeling and the assessment of passive cooling strategies in buildings [23,24].

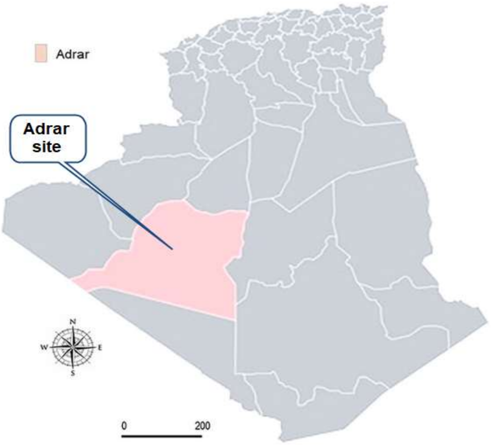

Fig. 3.1. Geographical location of the study area [22]

As shown in Figure 3.2, Adrar exhibits very mild winters and extremely hot, sunny summers. The city experiences a maximum average temperature of 46 °C in July, making it one of the hottest cities in the world. In July 2023, temperatures peaked at 49.9 °C, while in August 2023, a day was recorded with a minimum of 35.5 °C and a maximum of 49.8 °C [25].

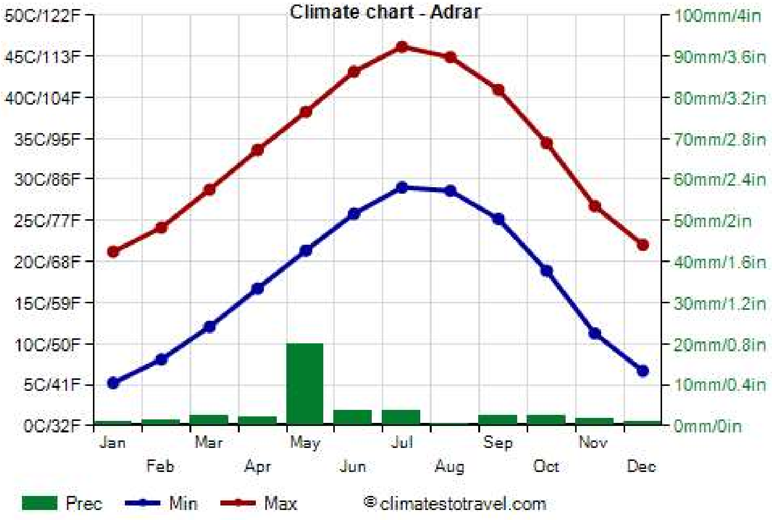

Fig. 3.2. Evolution of the average seasonal temperature range at the Adrar region in 2023 [25]

4. TEMPERATURE MEASUREMENT DEVICES

Temperatures were measured and recorded continuously every 24 hours over a period of 20 consecutive days in the workplace using Testo devices, as shown in Figure 4.1. Measurements were performed on the interior surfaces of the south and north walls, the roof, as well as in the indoor air volume, with additional recordings of the outdoor air temperature. The instrumentation provided high-resolution data with a precision of ±0.1 °C for temperature and ±2 % for relative humidity, ensuring accurate input for thermal modeling.

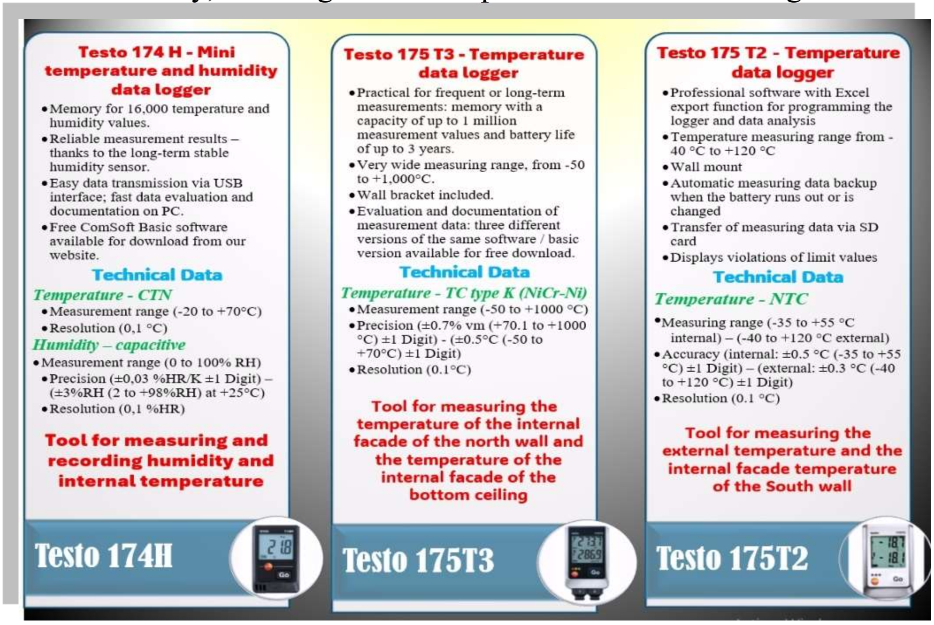

Testo 174 H - Mini temperature and humidity data logger

- Memory for 16,000 temperature and humidity values.
- Reliable measurement results – thanks to the long-term stable humidity sensor.
- Easy data transmission via USB interface; fast data evaluation and documentation on PC.
- Free ComSoft Basic software available for download from our website.

Technical Data

Temperature - CTN

- Measurement range (-20 to +70°C)
- Resolution (0,1 °C)

Humidity – capacitive

- Measurement range (0 to 100% RH)
- Precision (±0,03 %HR/K ±1 Digit) – (±3%RH (2 to +98%RH) at +25°C)
- Resolution (0,1 %HR)

Tool for measuring and recording humidity and internal temperature

Testo 174H

Testo 175 T3 - Temperature data logger

- Practical for frequent or long-term measurements: memory with a capacity of up to 1 million measurement values and battery life of up to 3 years.
- Very wide measuring range, from -50 to +1,000°C.
- Wall bracket included.
- Evaluation and documentation of measurement data: three different versions of the same software / basic version available for free download.

Technical Data

Temperature - TC type K (NiCr-Ni)

- Measurement range (-50 to +1000 °C)
- Precision (±0.7% vm (+70.1 to +1000 °C) ±1 Digit) - (±0.5°C (-50 to +70°C) ±1 Digit)
- Resolution (0.1°C)

Tool for measuring the temperature of the internal facade of the north wall and the temperature of the internal facade of the bottom ceiling

Testo 175T3

Testo 175 T2 - Temperature data logger

- Professional software with Excel export function for programming the logger and data analysis
- Temperature measuring range from -40 °C to +120 °C
- Wall mount
- Automatic measuring data backup when the battery runs out or is changed
- Transfer of measuring data via SD card
- Displays violations of limit values

Technical Data

Temperature - NTC

- Measuring range (-35 to +55 °C internal) – (-40 to +120 °C external)
- Accuracy (internal: ±0.5 °C (-35 to +55 °C) ±1 Digit) – (external: ±0.3 °C (-40 to +120 °C) ±1 Digit)
- Resolution (0.1 °C)

Tool for measuring the external temperature and the internal facade temperature of the South wall

Testo 175T2

Fig. 4.1. Measuring and recording devices for different temperatures of the workplace

4.1. Simplifying Assumptions of the Experimental Process

To ensure the proper execution of the experiment, several simplifying assumptions were adopted, which can be summarized as follows:

- The outdoor air temperature is assumed to be equivalent to the ground temperature.

- Humidity effects are neglected due to the region’s persistent arid conditions.
- Heat transfer is considered to be unidirectional.

Figure 4.1.1 illustrates the locations of the measuring devices both inside and outside the workplace.

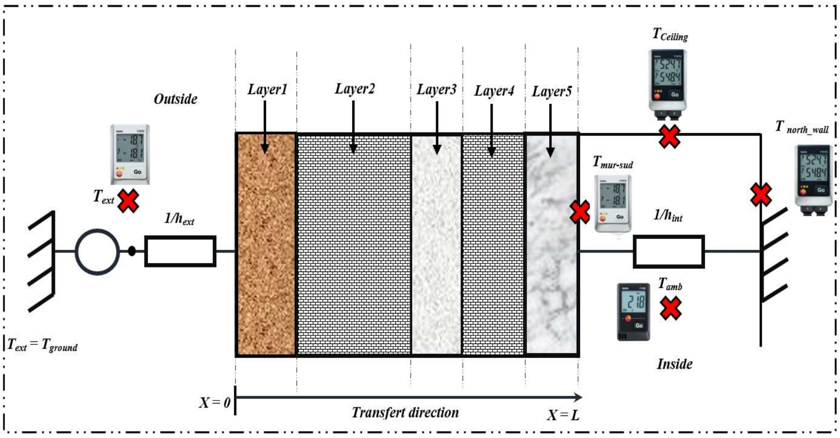

Fig. 4.1.1. Position of measuring devices inside and outside the workplace

5. MATHEMATICAL MODELLING OF THERMAL BEHAVIOUR

5.1. Loads Due to the Room Glazing

Glass walls are characterized by their absorption and transmission coefficients. Accordingly, the heat flux absorbed by a windowpane can be expressed by the following relation [26]:

$$Q_{ccv} = U_{\text{glas}} \times S_{\text{glas}} \times (T_{ext} - T_{\text{int}}) \tag{5.1.1}$$

In this context, the physical and thermal properties of the glass are considered, as summarized in Table 5.1.1.

Table 5.1.1. Physical and thermal properties of the glass of the workplace [27,28].

	$\lambda_{\text{glas}}\ (W.m^{-1}.K^{-1})$	$\rho_{\text{glas}}\ (Kg.m^{-3})$	$Cp_{\text{glas}}\ (J.Kg^{-1}.K^{-1})$	$U_{\text{glas}}\ (W.m^{-2}.K^{-1})$	$e_{\text{glas}}\ (Cm)$
Single Glass Window	1.05	2300	837	5.6	1

5.2. Loads due from the Workplace Door

The door in this workplace influences the internal heat exchange. The approximate amount of heat transferred through the door can be expressed by the following relation [29]:

$$Q_{\text{door}} = h_{conv} \times S_{\text{door}} \times \left(T_{ext} - T_{\text{int}}\right) \tag{5.2.1}$$

5.3. Thermal Convection Loads

- ***Convection Outside the Workplace***

In this case, the modeling focuses exclusively on heat transfer due to thermal convection through the five walls of the workplace, as described by the following relation [30-32]:

$$Q_{wall(i)} = h_{conv(ext)} \times S_i \times \left(T_{ext} - T_i\right) \tag{5.3.1}$$

The convective heat transfer coefficient on the exterior surfaces of the element is calculated using the following relation [33,34]:

$$h_{conv(ext)} = 5{,}7 + (3{,}8) \times V_{\text{wind}} \tag{5.3.2}$$

It was noted that the exterior façade of the south wall is the only surface directly exposed to solar radiation. Opaque materials are characterized by an absorption coefficient specific to visible radiation, and the net absorbed flux represents the corresponding heat source. By neglecting the portion of flux reflected back to the environment, the heat generated by these radiative exchanges is expressed by the following relation [33]:

$$Q_{absor} = Q_{source} = \sum_{i}^{n} \alpha_{i} \times S_{i} \times FSG(t) \tag{5.3.3}$$

- ***Convection in the workplace***

The thermal energy resulting from the heat exchange between the indoor air and the interior surfaces of the workplace walls is calculated using the following relation (Equation 5.3.4) [35,36]:

$$Q_{conv(wall)} = \sum_{i}^{n} h_{conv(\text{int})}.S_i.(T_{wall}^{i} - T_{amb}) \tag{5.3.4}$$

Natural convection occurs when a temperature gradient induces motion in the air, producing what are referred to as convective flows. Heat transfer within a fluid layer is governed both by thermal conduction and by the movement of the fluid. When a thermal gradient is applied across the surface layers, a corresponding density gradient develops [35]. Experimentally, it is observed that after a certain period, the fluid begins to move spontaneously, marking the onset of convection. This onset is characterized in Table 5.23.1 by a dimensionless parameter known as the Rayleigh (Ra) number [36].

Table 5.3.1. Expression of convective transfer coefficients [35,36].

Surface description	**Flow regime**	**Scope of validity** $Ra = Gr.\Pr$	**Expression**
Vertical wall	Laminar regime	$10^4 \langle Gr.\Pr \langle 10^9$	$h_{conv} = 1{,}42.\left(\Delta T / L\right)^{1/4}$
	Turbulent regime	$Gr.\Pr \rangle 10^9$	$h_{conv} = 1{,}31.\left(\Delta T / L\right)^{1/3}$
Upper surface of a horizontal hot plate or lower surface of a cold plate	Turbulent regime	$10^4 \langle Gr.\Pr \langle 10^9$	$h_{conv} = 1{,}32.\left(\Delta T / L\right)^{1/4}$
	Laminar regime	$Gr.\Pr \rangle 10^9$	$h_{conv} = 1{,}52.\left(\Delta T / L\right)^{1/3}$
Lower surface of a hot plate or upper surface of a cold plate	Turbulent regime	$10^4 \langle Gr.\Pr \langle 10^9$	$h_{conv} = 0{,}59.\left(\Delta T / L\right)^{1/4}$
	Laminar regime	$Gr.\Pr \rangle 10^9$	

5.4. Thermal Conduction Loads

Figure 5.4.1 presents a geometric schematic of the exterior south wall of the study element. It also illustrates the directions of heat transfer and thermal processes occurring within the wall materials.

For a linear temperature profile, the heat flux through the wall is calculated using the following relation [37,38]:

$$Q = -\lambda.S.\frac{dT}{dx} \tag{5.4.1}$$

In steady-state conditions, the heat flux through the wall is conserved and can be expressed using the following relation [39]:

$$Q = h_i.S.(T_{ext} - T_i) = \sum_{i=1}^{n} \frac{\lambda_i.S_i.(T_i - T_{i+1})}{e_i} = h_i.S_i.(T_i - T_{\text{int}}) \tag{5.4.2}$$

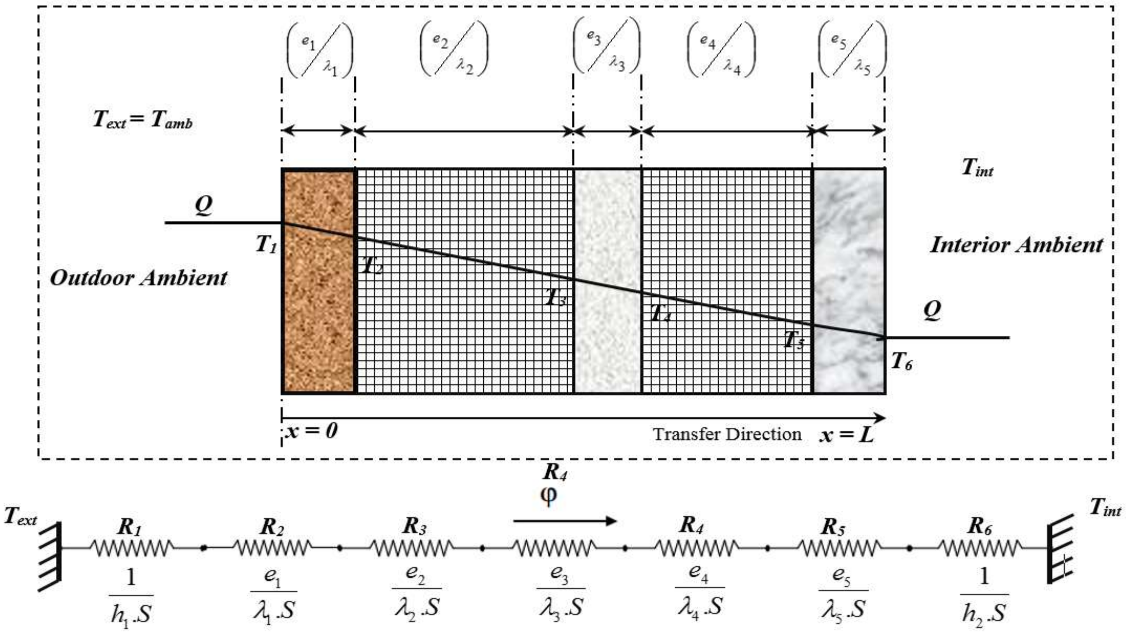

Fig. 5.4.1. Equivalent electrical diagram of a multilayer wall

5.5. Solar Radiation Loads

To consider the optical and geometric properties of the considered surfaces, the form factor *F'*$_{i+1}$ can be defined using the following expression [40]:

$$F'_{i\to i+1} = \left[\frac{1-\varepsilon_i}{\varepsilon_i} + \frac{1}{F_{i\to i+1}} + \frac{1-\varepsilon_{i+1}}{\varepsilon_{i+1}} \times \frac{S_i}{S_{i+1}}\right]^{-1} \tag{5.5.1}$$

The net radiative flux "$q_{r,i\,i+1}$" between the surfaces at temperatures "T_i" and "T_{i+1}", is expressed by the following relation [41]:

$$q_{r,i\to i+1} = S_i \times F'_{i\to i+1} \times \sigma \times \left(T_i^4 - T_{i+1}^4\right) \tag{5.5.2}$$

In linearized form, $q_{r,i+1}$ is written in expression 5.5.3 as follows:

$$\varphi_{r,i\to i+1} = h_{r,i\to i+1} \times \left(T_i - T_{i+1}\right) \tag{5.5.3}$$

The general expression for the radiative heat transfer coefficient between surfaces *i* and *i+1* is given by the following relation [38-40]:

$$h_{r,i\to i+1} = \frac{\sigma \times \left(T_i^2 - T_{i+1}^2\right) \times \left(T_i + T_{i+1}\right)}{\frac{1-\varepsilon_i}{\varepsilon_i} + \frac{1}{F_{i\to i+1}} + \frac{1-\varepsilon_{i+1}}{\varepsilon_{i+1}} \times \frac{S_i}{S_{i+1}}} \tag{5.5.4}$$

5.6. Principle of Thermal Analysis by the Nodal Method

The nodal method is particularly well suited for simulating the thermal behavior of buildings. It enables a global representation of the entire structure, including fluid circuits, and allows problems of different physical nature to be solved within a unified framework [42,43]. Moreover, its computational cost and memory requirements are significantly lower compared to finite element analyses.

This approach offers sufficient flexibility to refine the mesh locally when necessary. Based on the thermal–electrical analogy, the nodal method consists in discretizing the physical system into a finite number of isothermal elementary volumes (nodes). The thermal response of the system is obtained by solving the set of energy conservation equations, with one governing equation associated to each node.

The thermal balance of node *i* which exchanges heat by conduction with node *j*, by convection with node *k*, by radiation with node *l*, by fluid transport with node *m*, and interacts with heat sources or sinks *n*, leads to the nonlinear differential equation expressed in relation 5.6.1 [43-45].

$$\left(\rho.V.Cp\right)_i.\frac{dT_i}{dt}=\underbrace{\frac{\lambda.S_{ij}}{l_{ij}}.\left(T_j-T_i\right)}_{Conduction}+\underbrace{h.S_{ik}.\left(T_k-T_i\right)}_{Convection}+\underbrace{\sigma.\varepsilon.S_i.F_{il}.\left(T_l^4-T_i^4\right)}_{Rayonnement}+\underbrace{\overset{*}{m}.Cp_i.\left(T_m-T_i\right)}_{Transport}+\underbrace{\sum_n Q_n}_{\text{Source}} \tag{5.6.1}$$

The solution of each governing equation yields the temperature of the corresponding node as well as the associated heat fluxes. In the nodal framework, the residential thermal system is represented analogously to an electrical network: the thermal inertia of each node is modeled by a thermal capacitance, conductive and convective exchanges are represented by thermal conductances, imposed temperatures correspond to potential (voltage) nodes, and imposed heat flows are treated as current sources. Under this analogy, the global set of coupled nonlinear equations describing the system can be written in the compact matrix form expressed in relation 5.6.2 [45-47].

$$C_i.\frac{dT_i}{dt}=Q_{cond(j)}.\left(T_j-T_i\right)+Q_{conv(j)}.\left(T_k-T_i\right)+Q_{Ray(l)}.\left(T_l-T_i\right)+Q_{fluid(m)}.\left(T_m-T_i\right)+Q_{source} \tag{5.6.2}$$

5.7. Thermal Balance of Study Element

The thermal balance represents an evaluation of all energy inputs and outputs associated with the studied element over a defined time interval [33, 34]. The mathematical model developed for the thermal analysis was validated using experimental measurements, as detailed in the section dedicated to physical results and interpretation.

In accordance with the nodal modelling approach, each wall of the structure is treated as an individual node, and a specific thermal balance is established to describe all heat transfer mechanisms acting within that wall. Given that the studied enclosure comprises five walls, the resulting system of equations includes ten coupled thermal balance equations, to which an additional equation describing the natural convection of the confined indoor air must be added. Relations 5.7.1 and 5.7.2 illustrate representative equations of the global system obtained through numerical modelling in this study [45].

- *Thermal balances of exterior facades of the workplace*

In this configuration, the global energy balance comprises five independent equations, each associated with one of the external façades of the workplace, which exchange heat with the outdoor environment. Each equation explicitly accounts for the local climatic boundary conditions, as well as the thermal and physical properties of the construction materials constituting the corresponding façade.

$$\left\{\begin{array}{l}
\frac{m_{PS}.C_{P(PS)}}{S_{PS}}.\frac{\Delta T_{PSE}}{\Delta t}=h_{C(ext)}.\Delta T+\frac{\lambda_{PS}}{S_{PS}}.\Delta T+h_{r(VC,PSE)}.\Delta T+h_{r(SOL,PSE)}.\Delta T+\alpha_{PS}.\varphi_{PSE}\\
\frac{m_{PN}.C_{P(PN)}}{S_{PN}}.\frac{\Delta T_{PNE}}{\Delta t}=h_{C(ext)}.\Delta T+\frac{\lambda_{PN}}{e_{PN}}.\Delta T+h_{r(VC,PNE)}.\Delta T+h_{r(SOL,PNE)}.\Delta T++\alpha_{PN}.\varphi_{PNE}\\
\frac{m_{PO}.C_{P(PO)}}{S_{PO}}.\frac{\Delta T_{POE}}{\Delta t}=h_{C(ext)}.\Delta T+\frac{\lambda_{PO}}{e_{PO}}.\Delta T+h_{r(VC,POE)}.\Delta T+h_{r(SOL,POE)}.\Delta T+\alpha_{PO}.\varphi_{POE}\\
\frac{m_{PFP}.C_{P(PFP)}}{S_{PFP}}.\frac{\Delta T_{PFPE}}{\Delta t}=h_{C(ext)}.\Delta T+\frac{\lambda_{PFP}}{e_{PFP}}.\Delta T+h_{r(VC,PFPE)}.\Delta T+h_{r(SOL,PFPE)}.\Delta T+\alpha_{PFP}.\varphi_{PFPE}\\
\frac{m_{PE}.C_{P(PE)}}{S_{PE}}.\frac{\Delta T_{PEE}}{\Delta t}=h_{C(ext)}.\Delta T+\frac{\lambda_{PE}}{e_{PE}}.\Delta T+h_{r(VC,PEE)}.\Delta T+h_{r(SOL,PEE)}.\Delta T+\alpha_{PE}.\varphi_{PEE}
\end{array}\right\} \tag{5.7.1}$$

- *Thermal balance of interior facades of the workplace*

Similarly, the internal energy balance of the workplace considered in this study was established. It consists of six governing equations, each describing the heat transfer mechanisms acting on the internal façades of the enclosure. These equations account for convective, conductive, and radiative exchanges occurring between the indoor air and the corresponding internal surfaces.

$$\left\{\begin{array}{l}
\frac{m_{PS}.C_{P(PS)}}{S_{PS}}.\frac{\Delta T_{PSI}}{\Delta t}=h_{C(int)}.\Delta T+\frac{\lambda_{PS}}{e_{PS}}.\Delta T+h_{r(PSI,PNI)}.\Delta T+h_{r(PSI,POI)}.\Delta T+h_{r(PSI,PEI)}.\Delta T+h_{r(PSI,PFPI)}.\Delta T+h_{r(PSI,PP)}.\Delta T \\
\frac{m_{PN}.C_{P(PN)}}{S_{PN}}.\frac{\Delta T_{PNI}}{\Delta t}=h_{C(int)}.\Delta T+\frac{\lambda_{PN}}{e_{PN}}.\Delta T+h_{r(PNI,PSI)}.\Delta T+h_{r(PNI,PEI)}.\Delta T+h_{r(PNI,POI)}.\Delta T+h_{r(PNI,PFPI)}.\Delta T+h_{r(PNI,PP)}.\Delta T \\
\frac{m_{PO}.C_{P(PO)}}{S_{PO}}.\frac{\Delta T_{POI}}{\Delta t}=h_{C(int)}.\Delta T+\frac{\lambda_{PO}}{e_{PO}}.\Delta T+h_{r(POI,PSI)}.\Delta T+h_{r(POI,PNI)}.\Delta T+h_{r(POI,PEI)}.\Delta T+h_{r(POI,PFPI)}.\Delta T+h_{r(POI,PP)}.\Delta T \\
\frac{m_{PFP}.C_{P(PFP)}}{S_{PFP}}.\frac{\Delta T_{PFPI}}{\Delta t}=h_{C(int)}.\Delta T+\frac{\lambda_{PFP}}{e_{PFP}}.\Delta T+h_{r(PFPI,PSI)}.\Delta T+h_{r(PFPI,PNI)}.\Delta T+h_{r(PFPI,POI)}.\Delta T+h_{r(PFPI,PEI)}.\Delta T+h_{r(PFPI,PP)}.\Delta T \\
\frac{m_{PE}.C_{P(PE)}}{S_{PE}}.\frac{\Delta T_{PEI}}{\Delta t}=h_{C(int)}.\Delta T+\frac{\lambda_{PE}}{e_{PE}}.\Delta T+h_{r(PEI,PSI)}.\Delta T+h_{r(PEI,POI)}.\Delta T+h_{r(PEI,PNI)}.\Delta T+h_{r(PEI,PFPI)}.\Delta T+h_{r(PEI,PP)}.\Delta T \\
\frac{m_{air}.C_{P(air)}}{S_{air}}.\frac{\Delta T_{air}}{\Delta t}=h_{C(PSI,air)}.\frac{S_{PS}}{S_{air}}.\Delta T+h_{C(PNI,air)}.\frac{S_{PN}}{S_{air}}.\Delta T+h_{C(POI,air)}.\frac{S_{PO}}{S_{air}}.\Delta T+h_{C(PEI,air)}.\frac{S_{PE}}{S_{air}}.\Delta T+h_{C(PFPI,air)}.\frac{S_{PFP}}{S_{air}}.\Delta T+h_{C(PP,air)}.\frac{S_{PP}}{S_{air}}.\Delta T
\end{array}\right\} \quad (5.7.2)$$

Processing of Input and Output Data

Figure 5.8.1 illustrates the detailed computational flowchart employed for the numerical simulation. The diagram details the sequential operations implemented to evaluate the heat transfer mechanisms occurring within and around the workplace over a 24-hour representative cycle. The resulting system of linearized equations obtained from the numerical model was solved using the Gauss elimination algorithm.

The flowchart also clearly specifies the input parameters required at the initialization stage of the simulation, as well as the output variables produced at each iteration. It is important to highlight that the computation relies on time-averaged boundary and operating conditions, defined over discrete intervals throughout the day.

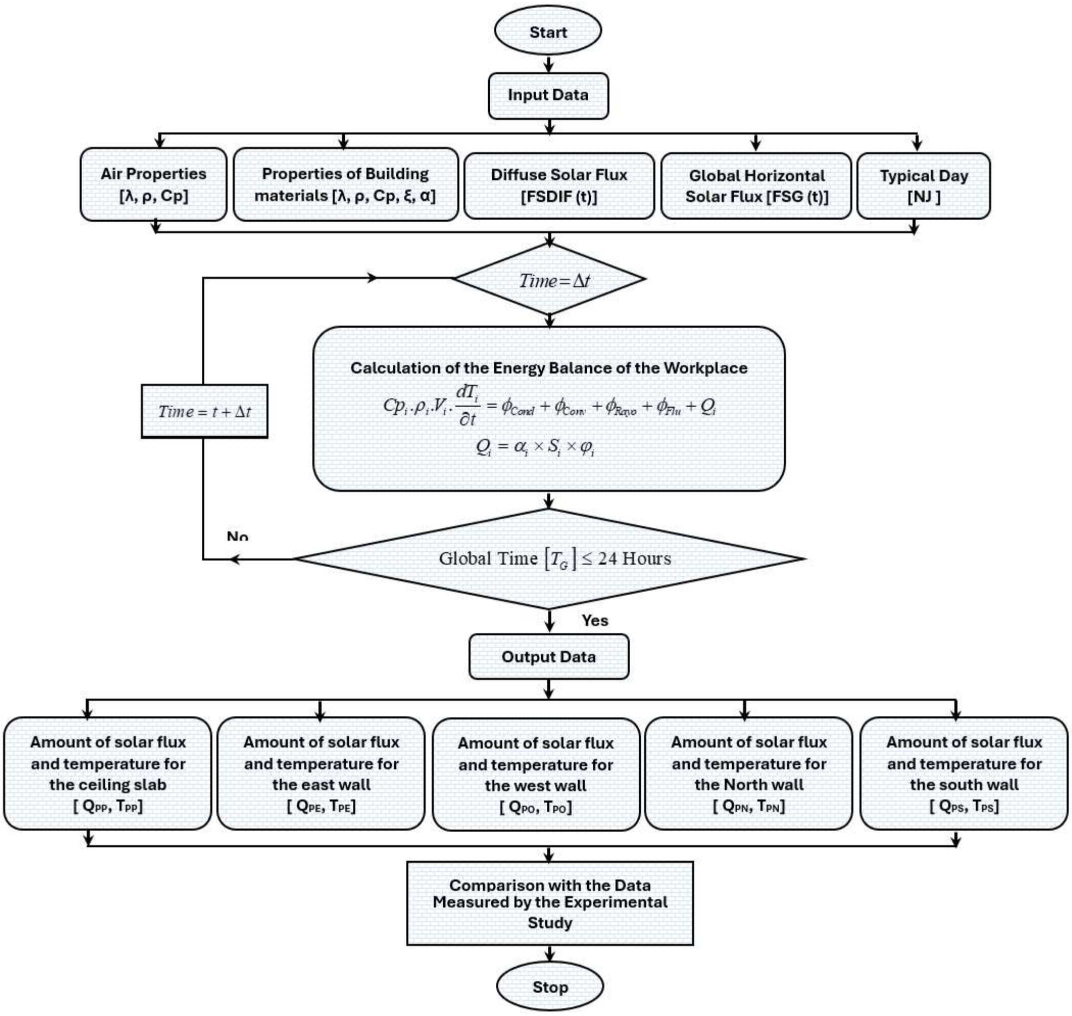

Fig. 5.8.1. Computational flowchart of the numerical heat transfer modeling

6. RESULTS AND DISCUSSION

6.1. Validation of the Developed Numerical Model

The validation of the numerical model developed in this study, based on data from two representative days, May 10th and May 18th, is presented in Figure 6.1.1. The results show a good agreement between the measured and simulated temperatures. Validation was performed for the following temperature types: T_{PN} (Figure 6.1.1a, May 18th, 2024), T_{in} (Figure 6.1.1b, May 18th, 2024; Figure 6.1.1c, May 10th, 2024), and T_{ext} (Figure 6.1.1d, May 10th, 2024), with all comparisons yielding satisfactory results. These findings confirm that the developed numerical model is valid and can be reliably used to simulate other thermal quantities, such as the temperature of wall façades and the solar flux incident on both the exterior and interior surfaces of the workplace. The maximum discrepancy between measured and calculated temperatures over the two selected days did not exceed 4%, further demonstrating the model's accuracy.

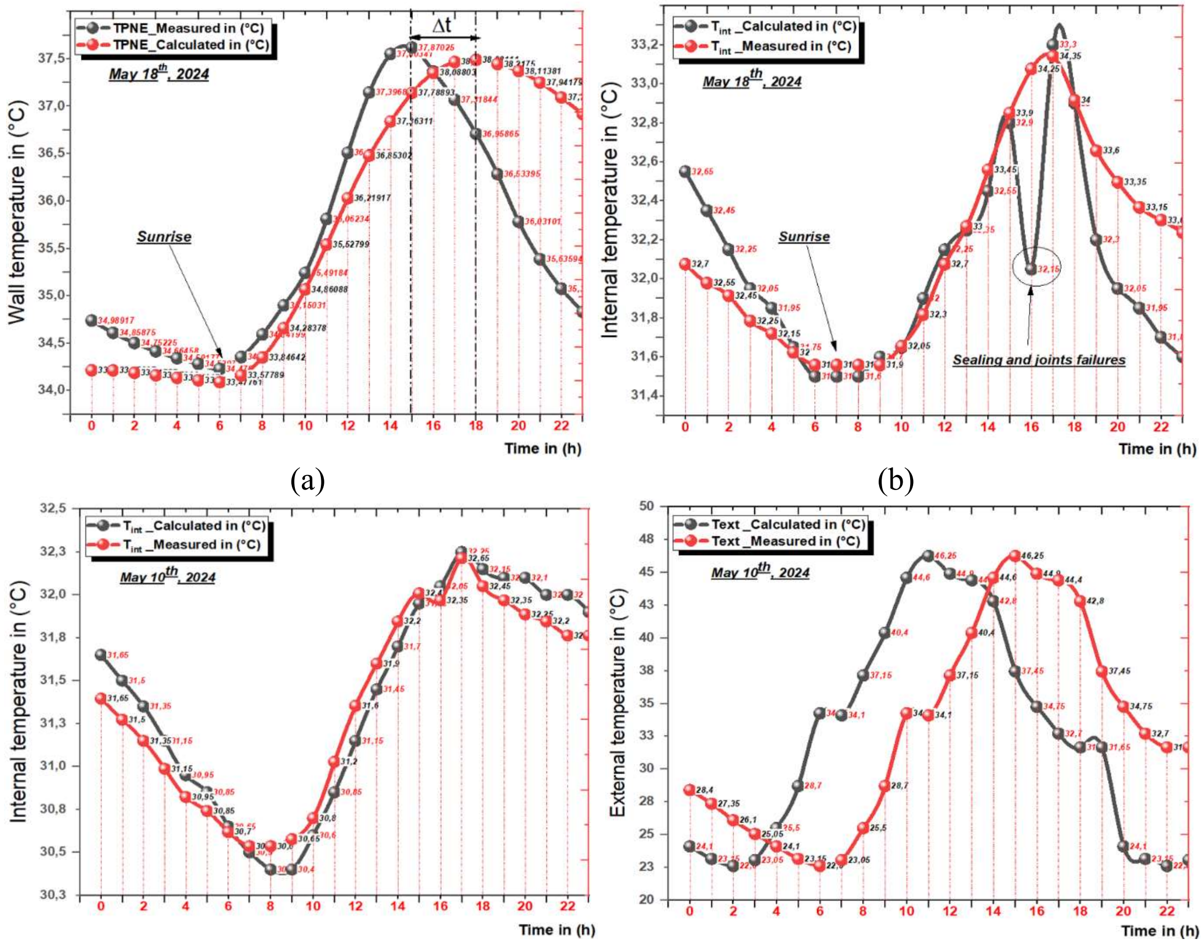

(a) (b)

(c) (d)

Fig. 6.1.1. Comparison between the measured temperature variations and the calculated temperature.

6.2. Analysis of Experimental Data

Figure 6.2.1 illustrates the temporal evolution of the external T_{ext} and internal T_{int} temperatures as a function of local time over the course of the experimental period. Figure 6.2.1(a) presents the variation of the external temperature T_{ext} at the study site over seven selected days. It can be observed that the daily external temperature profiles exhibit a similar pattern throughout the week. During the night, from the early hours until sunrise at around 8:00 a.m., T_{ext} ranges from 16.3°C (May 1st, 2024) to 31.8°C (May 20th, 2024). Following sunrise, the temperature gradually increases, reaching a peak in the late afternoon, approximately 5:00 p.m., with maximum values ranging from 40.31°C on May 1st, 2024, to 49.25°C on May 13th, 2024. Thereafter, the temperature gradually decreases and stabilizes within a limited range between 22.9°C (May 1st, 2024) and 31.0°C (May 13th, 2024). The average external temperature over the seven selected days is approximately T_{ext} (average) = 45.7°C.

Figure 6.2.1(b) shows the internal temperature T_{int} evolution at the study location as a function of local time. The results indicate that the internal temperature profiles for the seven days follow a similar daily trend. Notably, on May 1st and May 2nd, 2024, T_{int} exhibits slightly lower values compared to the other selected days. The maximum internal temperature reached T_{int} = 30.1°C at 6:00 p.m. on May 1st and 2nd, whereas for the remaining days, the peak internal temperature was T_{int} = 33.5°C at approximately 1:00 p.m. These observations indicate that the average internal temperature during early May in this desert region is relatively moderate but shows a gradual increase over the course of the month.

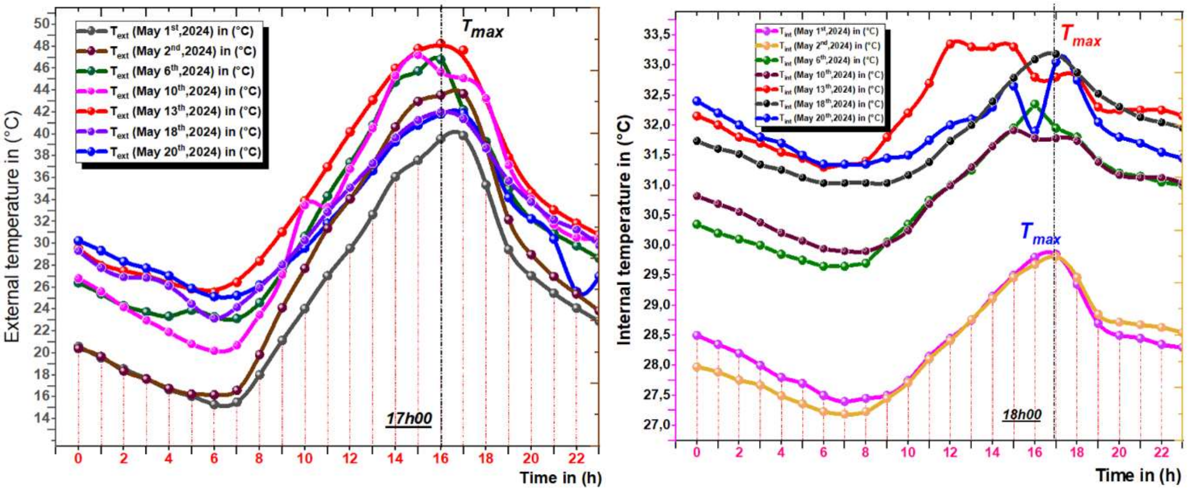

(a) (b)

Fig. 6.2.1. Evolution of external and internal temperature as a function of local time for different days of the experiment.

6.3. Analysis of Typical Day May 1st, 2024

Figure 6.3.1 illustrates the temporal evolution of the thermal behavior of the study site over a typical day, May 1st, 2024, as a function of local time. Figure 6.3.1(a) presents the variations of the internal air temperature T_{int} and relative humidity (RH) throughout the day. It is observed that T_{int} and RH follow a similar trend until approximately 10:00 a.m. From 1:00 p.m. onward, the relative humidity begins to evolve inversely with respect to the internal temperature: as T_{int} increases, RH decreases, reaching a maximum temperature of T_{int} = 30°C at 6:00 p.m. and a minimum relative humidity of RH = 15.5%. Figure 6.3.1(b) shows the comparison between the indoor T_{int} and outdoor T_{ext} air temperatures. Both quantities exhibit similar diurnal patterns, with a maximum of T = 41°C at 6:00 p.m. and a minimum of T = 15°C at 8:00 a.m. Figure 6.3.1(c) presents the evolution of the internal air temperature T_{int} along with the temperatures of the selected internal wall façades measured during the experiment. The temperature profiles of the walls follow the same general trend as T_{int}, with a minimum of T_{PFPI} = 27.3°C recorded at the lower inner ceiling façade at 6:00 p.m. and a maximum of T_{PSI} = 29.8°C at 10:00 p.m. on the inner south wall façade. A noticeable time lag of approximately Δt = 5 h is observed between the peak of the south wall inner façade temperature and the other temperatures T_{PNI}, T_{int} and T_{PFPI}. This lag is attributed to the thermal inertia of the building materials, their heat storage capacity, and delayed heat release.

Figure 6.3.1(d) compares the external temperature T_{ext} with the temperatures of the internal wall façades selected for measurement. The peak temperature of the inner south wall façade

T_{PSI} = 29.65°C occurs at 2:00 a.m., showing a time difference of Δt = 4 h relative to the other measured temperatures T_{PNI}, T_{ext} and T_{PFPI}. The minimum external temperature of T_{ext} = 16.3°C is recorded at 7:00 a.m. These observations highlight the significant role of material properties in inducing a time lag (Δt) between the internal south wall surface and other measured temperatures, reflecting the impact of thermal inertia and heat storage on the dynamic thermal response of the building.

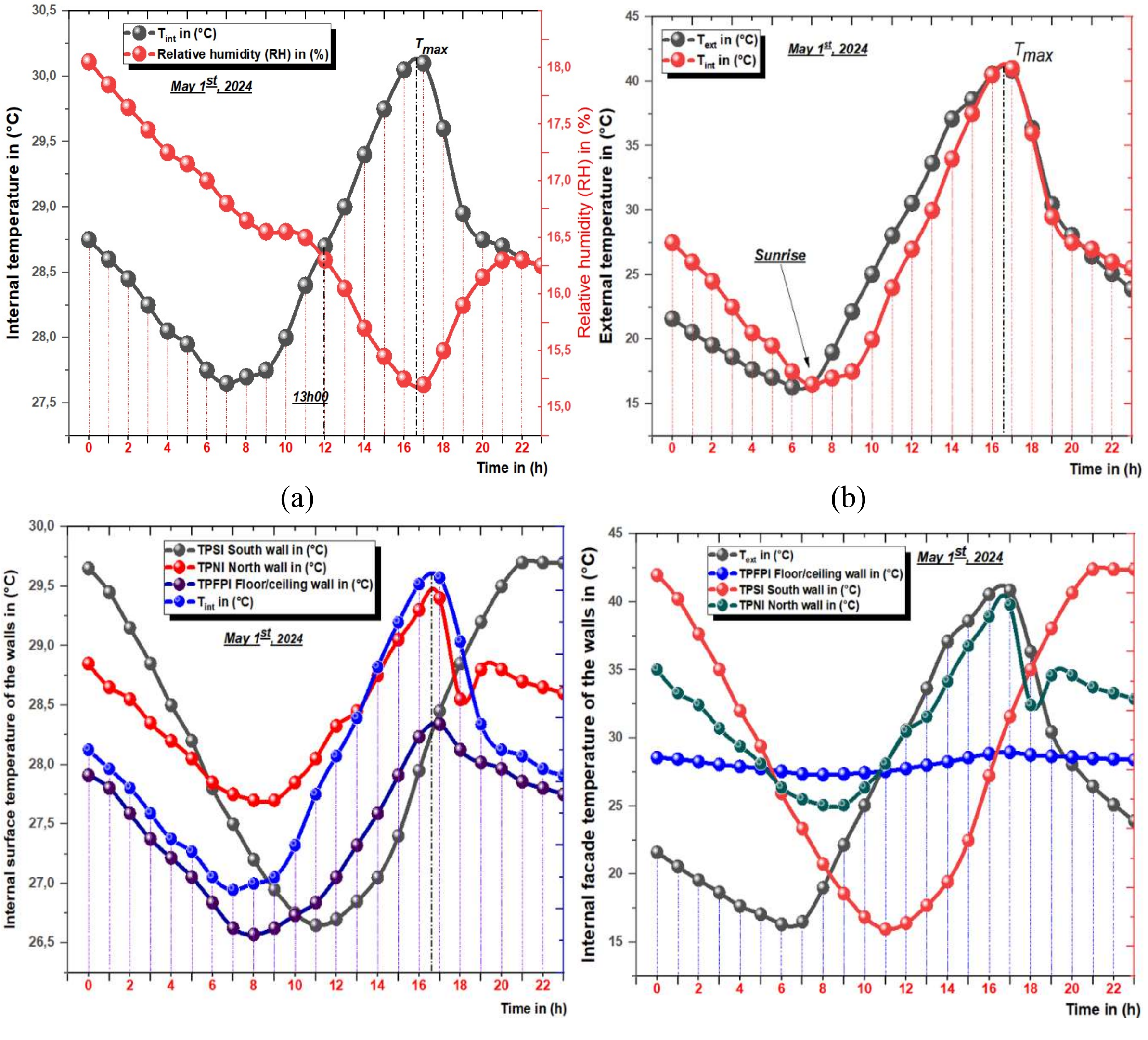

(a) (b)

(c) (d)

Fig. 6.3.1. Evolution of the thermal behavior of the element studied as a function of local time during the typical day May 1st, 2024.

6.4. Analysis of the Typical Day May 10th, 2024

Figure 6.4.1 illustrates the temporal evolution of the thermal behavior of the study site during a typical day, May 10th, 2024. Figure 6.4.1(a) presents the comparison between internal air temperature T_{int} and internal relative humidity (RH) as a function of local time. The results indicate an inverse relationship between T_{int} and RH throughout the day. Before noon, the minimum internal temperature of T_{int} = 30.6°C is observed at 8:00 a.m., while the relative humidity reaches a maximum of RH = 16.5%. In the afternoon, this trend reverses: T_{int} peaks at 32.9°C and RH reaches a minimum of 14.9% at 4:00 p.m., confirming the expected inverse correlation between internal temperature and relative humidity.

Figure 6.4.1(b) compares the internal T_{int} and external T_{ext} air temperatures throughout the day. Both temperatures follow a similar diurnal trend, with a maximum of T = 46.5°C recorded at 4:00 p.m. and a minimum of T = 22°C at 8:00 a.m. A temperature difference of ΔT = 4°C is observed between T_{int} and T_{ext} between 11:00 p.m. and midnight, explaining the higher internal temperature relative to the external environment during this period.

Figure 6.4.1(c) shows the comparison between the internal temperature T_{int} and the temperatures of the selected internal wall façades T_{PSI}, T_{PFPI} and T_{PNI} over the day. A temperature difference of $\Delta T = 1.6°C$ is observed between the north wall inner façade T_{PNI}, the roof inner façade T_{PFPI}, and the internal air temperature T_{int}, indicating that the roof inner surface is hotter than the other façades in the afternoon. Additionally, the inner south wall façade reaches its peak temperature of $T_{PSI} = 33.6°C$ at 10:00 p.m., exhibiting a time lag of $\Delta t = 6$ h relative to the internal air temperature T_{int}, due to the thermal inertia of the southern wall.

Figure 6.4.1(d) presents the comparison between external temperature T_{ext} and the selected internal wall temperatures T_{PSI}, T_{PFPI} and T_{PNI}. The south wall inner façade shows higher temperatures with a clear time lag of $\Delta t = 6$ h relative to T_{ext}, T_{PNI} and T_{FPI}. The outdoor temperature peaks at $T_{ext} = 45.7°C$ at 4:00 p.m., while the south wall inner surface reaches its maximum of $T_{PSI} = 33.6°C$ at 10:00 p.m. These observations highlight the influence of construction material properties, as the north wall and roof slab exhibit distinct thermal behavior compared to the south wall, due to differences in thermal inertia and heat storage capacity.

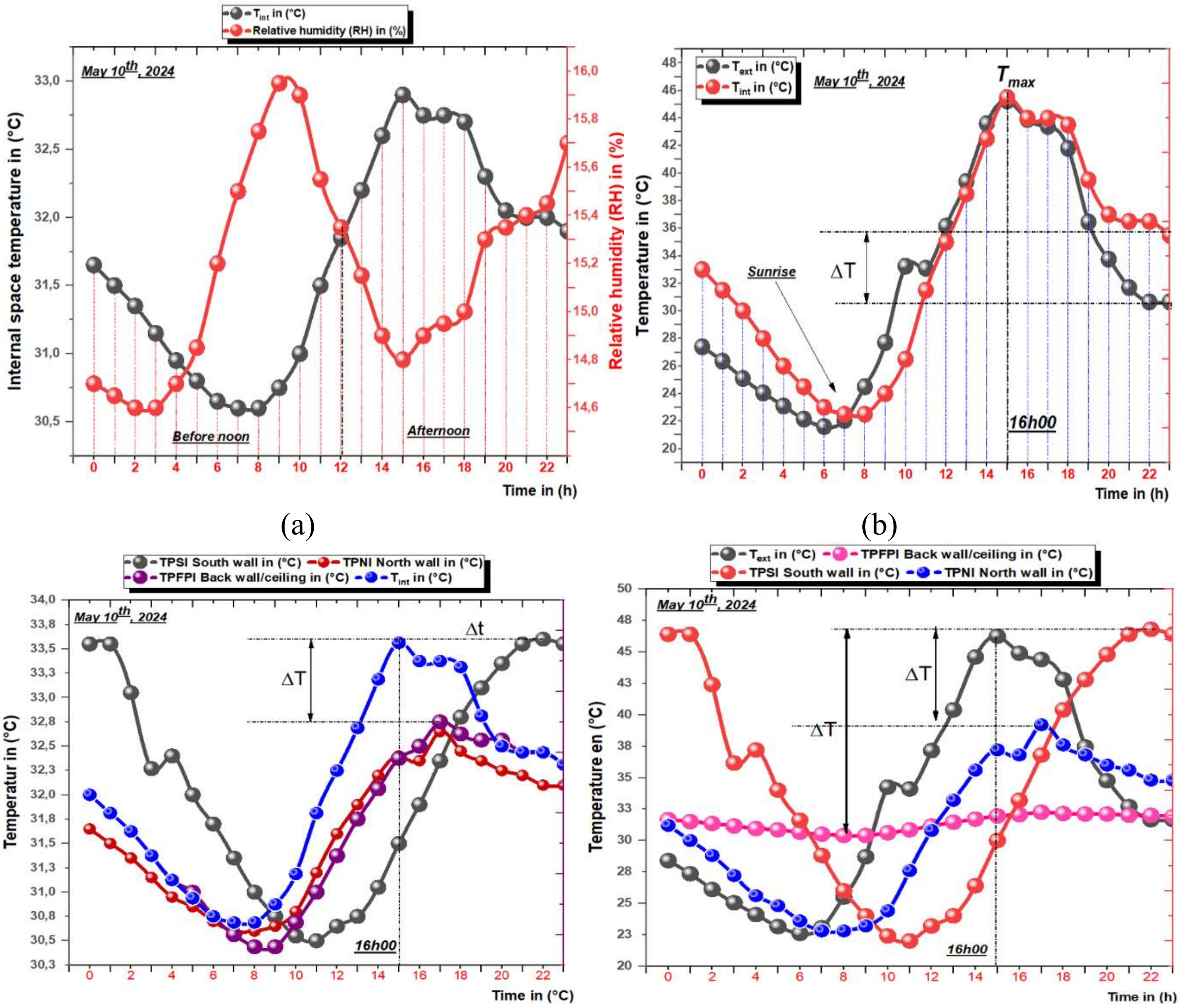

(a) (b)

(c) (d)

Fig. 6.4. Evolution of the thermal behavior of the element studied as a function of local time during the typical day May 10th, 2024.

6.5. Examination of a Week During the Experience Period

Figure 6.5.1 illustrates the evolution of the thermal behavior at the study site over a 7-day period, from May 1st to May 7th, 2024. Figure 6.5.1(a) presents the temporal variations of the internal air temperature T_{int}, external air temperature T_{ext}, and internal relative humidity (RH) as a function of local time. During this period, the maximum external temperature gradually increased, starting from $T_{ext} = 42.7°C$ on May 1st and reaching $T_{ext} = 50°C$ on May 7th. In contrast, the internal air temperature remained relatively stable, ranging between $T_{int} = 29°C$ and 33°C over the seven days. Meanwhile, the internal relative humidity exhibited a decreasing trend, from a maximum of RH = 16% on May 1st to RH = 13% by May 7th, reflecting the gradual increase in internal temperature.

Figure 6.5.1(b) shows the comparison between the temperatures of the selected internal wall façades T_{PSI}, T_{PFPI}, T_{PNI} and the external air temperature T_{ext} as a function of local time. The external temperature remains higher than the internal wall temperatures throughout the seven-day period. The north wall inner façade temperature remained relatively stable, between 23°C and 30°C, while the inner south wall and roof inner façade temperatures follow a similar trend, with a mean deviation of $\Delta T = 6°C$. These observations highlight the influence of wall orientation and material thermal properties on the thermal response of the building envelope.

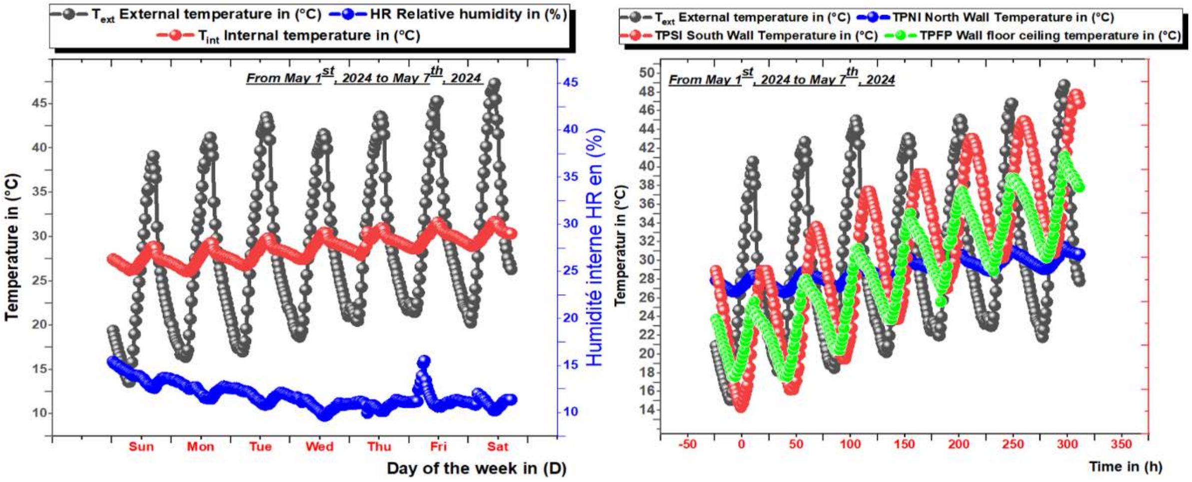

(a) (b)

Fig. 6.5.1. Evolution of temperature and relative humidity of the studied element during 7-days of experiment as a function of local time.

7. ANALYSIS AND INTERPRETATION OF COMPUTED THERMAL DATA

7.1. Effect of wall thickness on internal temperature variations

Figure 6.6.1 presents the temporal evolution of the internal air temperature T_{int} of the workplace as a function of wall thickness over a full diurnal cycle, corresponding to the sun's trajectory. The results demonstrate a clear inverse correlation between wall thickness and internal temperature, highlighting the thermal damping effect of increased wall mass. For a wall thickness of 0.15 m, the peak internal temperature reaches $T_{int,\,max} = 41°C$, whereas for 0.30 m, the peak decreases to $T_{int,\,max} = 36°C$. The observed temperature difference ($\Delta T = 5°C$) is associated with an estimated temporal phase shift of $\Delta t \approx 1$ h, indicating a delay in the thermal response of the internal environment due to the walls' heat storage capacity and thermal inertia. This behavior is consistent with nodal modeling predictions, where each wall is represented as a discrete thermal node with capacitance proportional to its mass and conductance defined by its thermal properties. The phase shift and amplitude attenuation of internal temperature underscore the critical role of wall thickness in modulating diurnal thermal fluctuations and controlling indoor thermal comfort under high solar loading conditions.

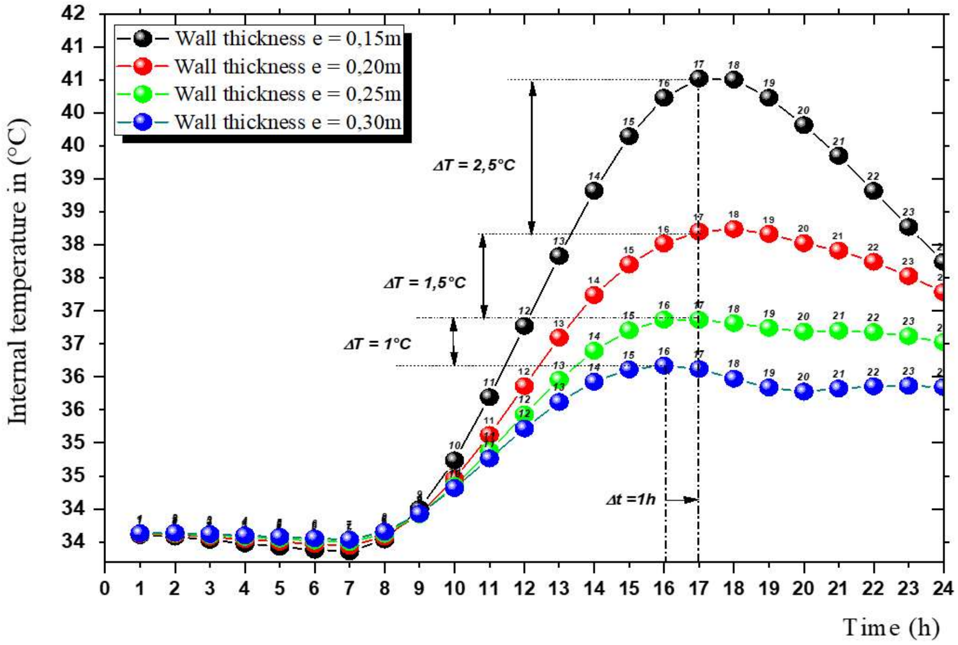

Fig. 6.6.1. Evolution in the temperature of the internal medium is a function of the evolution of the walls thickness.

7.2. Seasonal variation of the average external temperature in the year 2024

Figure 6.6.2 illustrates the annual evolution of the average outdoor temperature $T_{ext, avg}$ in the Adrar region during 2024. The temperature profile exhibits a distinct pyramidal seasonal pattern, with extreme values observed during summer and winter. Peak summer temperatures reach or exceed **50°C**, whereas winter minima range between 20°C and 22°C. Transitional seasons, spring and autumn, display intermediate average temperatures between 35°C and 40°C.

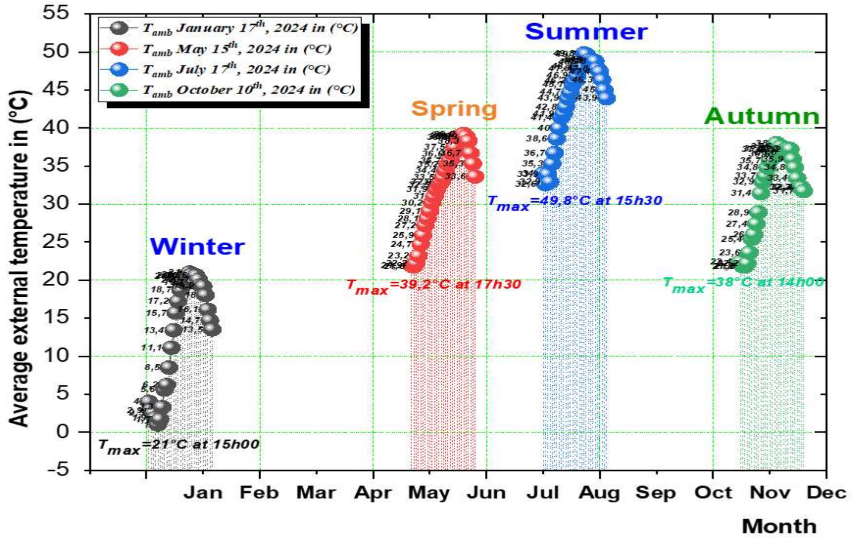

Fig. 6.6.2. Seasonal variation in the average outdoor temperature on 2024 depending on the year months.

These results confirm that the Adrar region is among the hottest regions globally, as evidenced by the extreme summer temperatures relative to other seasons. In nodal modeling of building envelopes, these external temperature variations serve as the primary driving forces for conduction, convection, and radiative exchanges, influencing both internal air temperatures and wall surface thermal responses. The extreme summer conditions further underscore the importance of accounting for thermal inertia, phase lag, and material-specific heat capacity in predicting internal thermal comfort and evaluating envelope performance.

7.3. Seasonal variation in the average global solar flux during the year 2024

Figure 6.6.3 shows the seasonal evolution of average solar irradiance for the year 2024. The irradiance exhibits consistent peak values across all seasons, ranging from 1000 W·m^{-2} to 11000 W·m^{-2}, with the maximum occurring in spring (11000 W·m^{-2}). These observations highlight the significant seasonal influence of solar radiation on the thermal loading of building envelopes, which is a critical boundary condition for heat transfer simulations and nodal thermal modeling. The high solar loading during peak periods underscores the importance of accounting for material thermal inertia and facade orientation in predicting indoor thermal behavior.

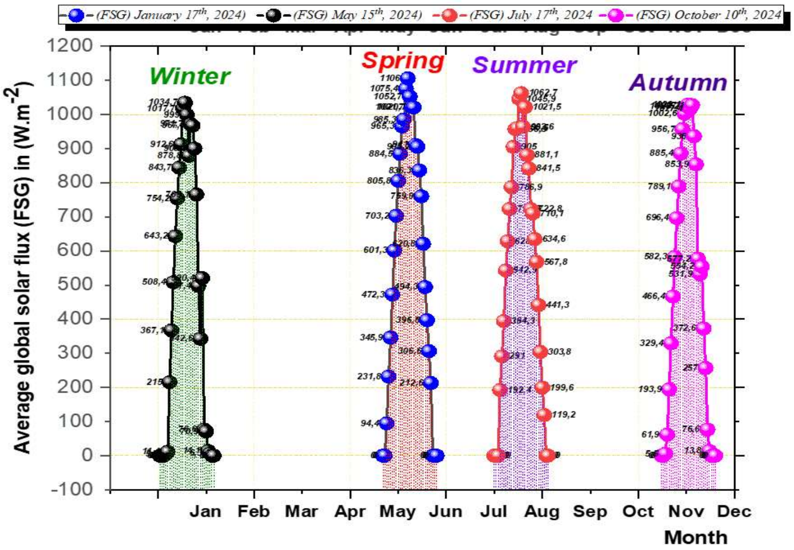

Fig. 6.6.3. Seasonal variation of the average solar flux in 2024 based on the year months.

8. CONCLUSION

This study combined experimental measurements and numerical simulations to analyze the thermal behavior of a workplace in Adrar. Wall temperatures and indoor relative humidity were recorded in May 2024 using Testo devices. The developed mathematical model accurately reproduced the experimental results, with an average error below 4%, validating its reliability for predictive thermal simulations.

Numerical analyses were extended to evaluate the influence of seasonal variations and material properties on internal temperatures over the entire year 2024. The main conclusions from this combined experimental and numerical study are as follows:

- The average outdoor temperature at the workplace in May 2024 ranged between 40°C and 45°C.
- The average internal temperature was maintained between 30°C and 35°C.
- The average internal relative humidity during the same period was approximately 13%.
- The temperature difference between the external environment and the interior surfaces of the workplace walls reached ≈6°C.

These results indicate that the internal thermal conditions are significantly higher than the ideal thermal comfort range. This can be attributed to extreme solar loading, low ambient humidity, and the thermal properties of the envelope.

As a future perspective, practical interventions are proposed to mitigate internal heat gains. Notably, the replacement of the existing air-gap insulation with locally available palm residue-based insulation is under investigation, aiming to enhance thermal damping and reduce peak internal temperatures under extreme climatic conditions.

ACKNOWLEDGMENT

We sincerely thank Professor Benaoumeur Aour, Head of the Laboratory of Applied Biomechanics and Biomaterials at the National Polytechnic School of Oran, for his guidance and thorough review of this project. Our gratitude also extends to Professor Hamouda Messaoud, Head of the Laboratory for Sustainable Development and Informatics (LDDI) at Adrar University, for his support in providing climate data for the Adrar region. We are furthermore grateful to the Algerian Directorate-General for Research and Technological Development (DGRST) for their encouragement and support throughout this research.

REFERENCES

1. Lalanne, N., Krapez, J., Niliot, C. & Briottet, X. (2013) Modeling of thermal behavior and high-resolution infrared rendering of external surfaces of an urban fragment and thermal bridges of buildings, *Proc. of French Thermal Congress* (Gérardmer, France).
2. Leschok, M., et al. (2024) Thermal and manufacturing properties of hollow-core 3D-printed elements for lightweight facades, *Developments in the Built Environment*, **19**, 100485. doi: 10.1016/j.dibe.2024.100485.
3. Zhou, H., Puttige, A. R., Nair, G. & Olofsson, T. (2024) Thermal behaviour of a gypsum board incorporated with phase change materials, *Journal of Building Engineering*, **94**, 109928. doi: 10.1016/j.jobe.2024.109928.
4. Oudrane, A. & Aour, B. (2017) Numerical Simulation of Heat Exchanges for a Desert House Type Adrar, *AEF*, **24,** 63–75. doi: 10.4028/www.scientific.net/aef.24.63.
5. Kumaraswamy, J., Vijay Praveen, P.M., Hassan A.H., Alzahrani, S., Sharma, V., et al. (2024) Experimental investigation of heat transfer rate for building roof with corrugated sheets using phase change material (PCM), *Case Studies in Thermal Engineering*, **59**, 104508. doi: 10.1016/j.csite.2024.104508.
6. Kaoutari, T. & Louahlia, H. (2024) Experimental and numerical investigations on the thermal and moisture transfer in green dual layer wall for building, *Case Studies in Thermal Engineering*, **53**, 103946. doi: 10.1016/j.csite.2023.103946.
7. Gori, V., Johnston, D., Bouchié, R. & Stamp, S. (2023) Characterisation and analysis of uncertainties in building heat transfer estimates from co-heating tests, *Energy & Buildings*, **295**, 113265. doi: 10.1016/j.enbuild.2023.113265.
8. Belatrache, D., Bentouba, S., Zioui, N. & Bourouis, M. (2023) Energy efficiency and thermal comfort of buildings in arid climates employing insulating material produced from date palm waste matter, *Energy*, **283**, 128453. doi: 10.1016/j.energy.2023.128453.
9. Laidi, S., El Hassar, S. M. K., Mahrane, A. & Sellami, R. (2024) Study and modeling of the thermal behavior of buildings with attic roof in the Algerian climate context, *International Journal of Sustainable Building Technology and Urban Development*, 3–22. doi: 10.22712/susb.20240002.
10. Jiang, B., Lua, R., Jiang, M., Wang, L., Chun, L., et al. (2024) Experimental study on thermal and humidity properties of modified rammed earth buildings in winter, *Building and Environment*, **258**, 111583. doi: 10.1016/j.buildenv.2024.111583.
11. Hou, C., Hu, W., Jiang, Y. F. & Gao, W. (2024) Optimization and Renovation Design of Indoor Thermal Environment in Traditional Houses in Northeast Sichuan (China) —A Case Study of a Three-Section Courtyard House, *Sustainability*, **16**, 2921, doi: 10.3390/su16072921.

12. Al-Yasiri, Q. & Szabob, M. (2023) Hourly analysis of temperature and heat gain reduction for building envelope-compacted phase change material in extremely hot conditions, *Journal of Energy Storage*, **68**, 107838, doi: 10.1016/j.est.2023.107838.

13. Yadeta, C., Indraganti, M., Tucho, G. T. & Alemayehu, E. (2023) Study on adaptive thermal comfort model and behavioral adaptation in naturally ventilated residential buildings, Jimma Town, Ethiopia, *Energy & Buildings*, **298**, 113483. doi: 10.1016/j.enbuild.2023.113483.

14. Guo, Y., Tang, H., Gao, Y., Wang, Y., Meng, X., et al. (2023) Thermal comfort and adaptive behaviors in office buildings: A pilot study in Turpan (China) during summer, *Heliyon 9*, e20646. doi: 10.1016/j.heliyon.2023.e20646.

15. Energie Plus (2024), [Online]. Available: https://energieplus-lesite.be/donnees/enveloppe44/enveloppe2/conductivite-thermique-des-materiaux/#Les_metaux

16. Cerezo, V. (2005). Mechanical, thermal and acoustic properties of a material based on plant particles: experimental approach and theoretical modeling. *Ph.D. Thesis*, National Institute of Applied Sciences of Lyon.

17. Bendahir, F. & Elfodda, K. (2017). *Master's thesis*, University of Adrar.

18. TAHITI Polynésie (2023) Application sheet for energy regulations for buildings in French Polynesia, [Online]. Available: https://www.developmentaid.org/donors/view/190456/energy-and-mining-service-french-polynesia-service-de-lenergie-et-des-mines-tahiti.

19. Loumani, A., Tahri, A., Mediani, A., Larbi, A., Braham, C. W., et al. (2022) Assessment Biodiversity of Medicinal Plants Used in Treatments for Native People in Adrar, Algeria, *International Journal of Design & Nature and Eco-dynamics*, **17**(3), 469–473. doi: 10.18280/ijdne.170319.

20. Mediani, A., Moungar, H., Larbi, A., Loumani, A., Chaouch, W.B., et al. (2019) The isothermal sorption measurement and the isosteric heats determinations for the South Algerian date varieties, *Instrumentation Mesure Métrologie*, **18**(4), 389–396. doi: 10.18280/i2m.180408.

21. Semmani, I., Elaloui, F. & Loumani, A. (2021) Microbiological and physicochemical assessment of mentha pulegium before and after solar drying, [Online]. Available: https://dspace.univadrar.edu.dz/jspui/handle/123456789/6127.

22. Danoune, M. B., Djafour, A., Hamouda, M., Degla, A., Gougui, A., et al. (2023) A Technical and Economical Assessment of Hydrogen Production Potential from Solar Energy in Adrar, Algeria, *Proc. of the second International Conference on Energy Transition and Security* (Adrar, Algeria). doi: 10.1109/ICETS60996.2023.10410685.

23. Benmedjahed, M., Dahbi, A., Hadidi, A. & Mouhadjer, S. (2021) Temperature and Wind Distribution Effects on Wind Energy Production in Adrar Region (Southern Algeria), *International Journal of Sustainable Development and Planning*, **16**(8), 1473–1477. doi: 10.18280/ijsdp.160808.

24. Peel, M. C., Finlayson, B. L. & McMahon, T. A. (2007). Updated world map of the Köppen-Geiger climate classification, *Hydrology and Earth System Sciences Discussions*, **4**(2), 439–473. doi: 10.5194/hess11-1633-2007.

25. Climates for traveling. Global Climate Guide, [Online]. Available: https://www.climatestotravel.com/info/contact

26. Bouitna, M. (2014). Study of the contribution of phase change materials for passive air conditioning. *Master's Thesis*, University of Blida in Algeria.

27. Morel N. & Gnansounou, E. (2007). *Building energy. New edition of the course previously given by Claude-Alain Roulet and Arnaud Dauriat*. Lausanne, France: Federal Institute of Technology in Lausanne.

28. Penu, G. (2013) Building thermal. Dunod. Paris, France: Dunod.

29. Boukli, M. A. H., Amara, S. & Chabane, N. E. S. (2011) Thermal requirements and temperatures evolution in an ecological house, *Energy Procedia*, **6**, 1–5. doi: 10.1016/j.egypro.2011.05.013.

30. Katunsky, D., Katunskà, J., Dolnikovà, E., et al. (2024) Preserving the historical value and thermal properties of renovated. buildings: The case of reconstructed town houses in Kosice, Slovakia, *Frontiers of Architectural Research*, **13**(1). doi: 10.1016/j.foar.2024.04.007.

31. Lin, Y. J., et al. (2013) Design of a sustainable planting module for extensive green roofs in tropical climate, *Advanced Materials Research*, **650**, 677–680. doi: 10.4028/www.scientific.net/amr.650.677.

32. Saikrishnan, V., Jagadeesh, P. & Jayasuriyaa, K. (2015) Experimental investigation of solar paraffin wax melting unit integrated with phase change heat energy storage by using phase change material, *AMM*, **766–767**, 451–456. doi: 10.4028/www.scientific.net/amm.766-767.451.

33. Oudrane, A. & Aour., B. (2019) Study and characterization of thermal comfort in a desert climate, *Adv. Syst. Sci. Appl.*, **19**(2), 63–79.

34. Ding, K., Calautit, J. K. & Jimenez-Bescos, C. (2024) Significance of external wind conditions on the convective heat transfer coefficients (CHTC) and energy performance in multi-zone high-rise buildings, *Energy & Buildings*, **320**, 114570. doi: 10.1016/j.enbuild.2024.114570.

35. Oudrane, A., Aour, B., Hamouda, M., Mokretar, S. El & Benhamou, M. (2018) Thermal exchanges of the walls of a habitable environment: study and analysis, *Renewable Energy Review*, **21**(2), 231–245. doi: 10.54966/jreen. v21i2.685.

36. Oudrane, A. (2018) Contribution to modeling and development of heating systems solar for individual use. *Ph.D. Thesis*, Oran Polytechnic School (ENPO-MA).

37. Ravello, B., Rajaoarisoab, L. & Maurice, O. (2020) Thermal modelling of multilayer walls for building retrofitting applications, *Journal of Building Engineering*, **29**, 101126. doi: 10.1016/j.jobe.2019.101126.

38. Zhakatayev, T., Kakimovab, K., Taukenovaa, L. & Serikovc, T. (2022) Simulation and calculation of heat transfer in multilayer wall structures based on iterative models, *Journal of Siberian Federal University. Engineering & Technologies*, **15**(5), 622–633. doi: 10.17516/1999-494X-0410.

39. Tamene, B. Y., Abboudi, S. & Bougriou, C. (2014) Numerical and economical study of thermal insulation in multi-layer wall exposed to real climatic conditions, *Athens Journal of Technology Engineering*, **1**(2).

40. Herrando, M., Markides, C. N. & Hellgardt, K. (2014) A UK-based assessment of hybrid PV and solar-thermal systems for domestic heating and power: System performance, *Applied Energy*, **122**, 288–309. doi: 10.1016/j.apenergy.2014.01.061.

41. Rahiminejad, M. & Khovalyg, D. (2022) Numerical and experimental study of the dynamic thermal resistance of ventilated air spaces behind passive and active facades, *Building and Environment*, **225**, 109616. doi: 10.1016/j.buildenv.2022.109616.

42. Charmantray, C. (2020) Transversalization of a nodal model of thermal behavior of a Diesel at low temperature in transient regime. *MEGA Doctoral School Thesis*, Central School of Lyon.

43. Kim, S., Joo, H. G. & Lee, H. C. (2024) Nodal method for handling irregularly deformed geometries in hexagonal lattice cores, *Nuclear Engineering and Technology*, **56**, 772–784. doi: 10.1016/j.net.2023.07.021.

44. Derakhtenjani, A. S., Candanedo, J. A., Chen, Y., Dehkordi, V. R. & Athienitis, A. K. (2015) Modeling approaches for the characterization of building thermal dynamics and model-based control: A case study, *Science and Technology for the Built Environment*, **21**, 824–836. doi: 10.1080/23744731.2015.1057060.

45. Oudrane, A., Aour, B. & Hmouda, M. (2022) The implementation of numerical codes for the analysis of solar flux inputs and the optimization of thermal comfort for a Monobloc habitat, *European Journal of Computational Mechanics*, **31**(2), 155–196. doi: 10.13052/ejcm2642-2085.3121.

46. Liu, W., Liu, X., Chow, T., Hao, Y., Lau, W., et al. (2024) Thermal characteristics of heat-pipe-ring embedded building facades as both building-integrated and building-attached solar collectors, *Case Studies in Thermal Engineering*, **60**, 104621. doi: 10.1016/j.csite.2024.104621.

47. Kaoutari, T. & Louahlia, H. (2024) Experimental and numerical investigations on the thermal and moisture transfer in green dual layer wall for building, *Case Studies in Thermal Engineering*, **53**, 103946. doi: 10.1016/j.csite.2023.103946.